PRELIMINARY COMPUTATIONAL ANALYSIS OF THE HIRENASD CONFIGURATION IN PREPARATION FOR THE AEROELASTIC PREDICTION WORKSHOP

Pawel Chwalowski, Jennifer P. Florance, Jennifer Heeg, Carol D. Wieseman, Boyd Perry, III[1]

[1]Aeroelasticity Branch
NASA Langley Research Center
Hampton, VA 23681
USA
Pawel.Chwalowski@nasa.gov, Jennifer.P.Florance@nasa.gov,
Jennifer.Heeg@nasa.gov, Carol.D.Wieseman@nasa.gov,
Boyd.Perry.iii@nasa.gov

Abstract: This paper presents preliminary computational aeroelastic analysis results generated in preparation for the first Aeroelastic Prediction Workshop (AePW). These results were produced using FUN3D software developed at NASA Langley and are compared against the experimental data generated during the HIgh REynolds Number Aero-Structural Dynamics (HIRENASD) Project. The HIRENASD wind-tunnel model was tested in the European Transonic Windtunnel in 2006 by Aachen University′s Department of Mechanics with funding from the German Research Foundation. The computational effort discussed here was performed (1) to obtain a preliminary assessment of the ability of the FUN3D code to accurately compute physical quantities experimentally measured on the HIRENASD model and (2) to translate the lessons learned from the FUN3D analysis of HIRENASD into a set of initial guidelines for the first AePW, which includes test cases for the HIRENASD model. This paper compares the computational and experimental results obtained at Mach 0.8 for a Reynolds number of 7 million based on chord, corresponding to the HIRENASD test conditions No. 132 and No. 159. Aerodynamic loads and static aeroelastic displacements are compared at two levels of the grid resolution. Harmonic perturbation numerical results are compared with the experimental data using the magnitude and phase relationship between pressure coefficients and displacement. A dynamic aeroelastic numerical calculation is presented at one wind-tunnel condition in the form of the time history of the generalized displacements. Additional FUN3D validation results are also presented for the AGARD 445.6 wing data set. This wing was tested in the Transonic Dynamics Tunnel and is commonly used in the preliminary benchmarking of computational aeroelastic software.

1 INTRODUCTION

The fundamental technical challenge in computational aeroelasticity is the accurate prediction of unsteady aerodynamic phenomena and their effect on the aeroelastic response of a vehicle. Currently, a benchmarking "standard" for use in validating the accuracy of computational aeroelasticity codes does not exist. Many aeroelastic data sets have been obtained in wind-tunnel and flight testing; however, none have been globally recognized as an ideal data set. There are numerous reasons for this. One is that often such aeroelastic data sets focus on the aeroelastic phenomena alone (flutter, for example) and do

not contain associated information, such as unsteady pressures or structural deflections. Other available data sets focus solely on the unsteady pressures and do not address the aeroelastic phenomena. Other deficiencies can include omission of relevant data, such as flutter frequency, or the acquisition of only qualitative deflection data. In addition to these content deficiencies, all of the available data sets present both experimental and computational technical challenges. Experimental issues include facility influences, nonlinearities beyond those being modeled, and data post processing. From the computational perspective, technical challenges include modeling geometric complexities, coupling between the flow and the structure, turbulence modeling, grid issues, and boundary conditions. An Aeroelasticity Benchmark Assessment task was initiated at NASA Langley in October 2009 with the primary objectives of (1) examining the existing potential experimental data sets and selecting the one(s) viewed as the most suitable for computational benchmarking and (2) performing an initial computational evaluation of these configurations using the NASA Langley-developed computational aeroelastic (CAE) software FUN3D [1] as part of its code validation process. A successful effort will result in the identification of a focus problem for government, industry, and academia to use in demonstrating and comparing codes, methodologies, and experimental data to advance the state of the art. Ideally, such a focus problem would be but the first of many put forth for this purpose, with a future goal being the design, fabrication, and testing of an aeroelastic model recognized by the community as a benchmark aeroelastic standard.

Excellent examples of such a progression and escalation of code validation in the international community are the series of four AIAA Drag Prediction Workshops (DPWs) [2] that have been held since 2001 and the AIAA High Lift Prediction Workshop (HiLiftPW) [3] that was held in 2010. These workshops had three main objectives. The first was to assess the ease and practicality of using state-of-the-art computational methods for aerodynamic load prediction. The second was to impartially evaluate the effectiveness of the Navier-Stokes solvers, and the final objective was to identify areas for improvement. The structure of the DPW and the HiLiftPW provides a template for other computational communities seeking similar improvements in accuracy within their own fields. The examination and selection of aeroelastic data sets within the Aeroelasticity Benchmark Assessment task together with the computational evaluation of these configurations led to initiation of an Aeroelastic Prediction Workshop (AePW) series [4].

The main focus of this paper will be on comparing the computational aeroelastic results generated using FUN3D software against the corresponding experimental data acquired during the HIgh REynolds Number Aero-Structural Dynamics (HIRENASD) project [5–7], which has also been selected to be part of the first AePW. This computational effort was performed to obtain a preliminary assessment of the ability of the FUN3D code to accurately compute quantities experimentally measured on the HIRENASD model and to begin the work of establishing guidelines for the AePW. A secondary intent of this paper is to show additional validation of FUN3D using the AGARD 445.6 wing data set, focusing on prediction of the flutter boundary.

Information relevant to the numerical methods employed will be presented first, including those for grid generation and rigid steady, static aeroelastic, forced oscillation, and dynamic aeroelastic analyses. Details associated with the AGARD 445.6 wing and HIRENASD analyses will then be presented.

2 NUMERICAL METHOD

2.1 Grid Generation

Unstructured tetrahedral grids used in this study were generated using VGRID [8] with input prepared using GridTool [9]. For the HIRENASD configuration, the boundary layer grid was converted into prism elements using preprocessing options within the FUN3D software. For the AGARD 445.6 wing grids, the boundary layer consisted of tetrahedral elements. Equation 1 describes the grid point distribution normal to the body, where Δ_n is the normal spacing of the nth layer, Δ_0 defines an initial cell height, and the variables r_1 and r_2 define the geometric growth rate and the exponential growth rate, respectively.

$$\Delta_n = \Delta_0[1 + r_1(1 + r_2)^{n-1}]^{n-1} \tag{1}$$

The off-surface length scale growth rate is governed by the parameters Γ_1 and Γ_2 according to the following equations:

$$\Delta s_{|\boldsymbol{r}|} = \Delta s_0 \left(1 + \frac{\Gamma_1}{a}\right)^{\eta} \tag{2}$$

where

$$\eta = \left(1 + \frac{|\boldsymbol{r}|}{\Delta \bar{s}}\Gamma_2\right) \frac{\ln\left(1 + \frac{|\boldsymbol{r}|\Gamma_1}{\Delta s_0 a}\right)}{\ln\left(1 + \frac{\Gamma_1}{a}\right)} \tag{3}$$

and Δs_0 is the primary grid spacing at the source, $\Delta s_{|\boldsymbol{r}|}$ is the primary grid spacing at the target point, η is the hybrid growth exponent, $|\boldsymbol{r}|$ is the euclidean distance between a target point and a source, a is the source strength, and $\Delta \bar{s}$ is the characteristic length (average mesh spacing) [8]. The magnitudes of the growth rate parameters used in this study are identified in specific sections of this paper describing analyzed configurations.

2.2 Rigid Steady Flow Analysis

Solutions to the Reynolds-Averaged Navier-Stokes (RANS) equations were computed using the FUN3D flow solver. Turbulence closure was obtained using either the Spalart-Allmaras [10] one-equation model or the shear-stress transport (SST) model by Menter [11]. Flux limitation was accomplished with either an augmented van Leer [12] or Venkatakrishnan [13] limiter. Inviscid fluxes were computed using either the Low-Diffusion Flux-Splitting Scheme (LDFSS) of Edwards [14] or the Roe scheme [15]. Unless stated otherwise, the solutions in this paper were obtained with an augmented van Leer limiter, LDFSS for inviscid fluxes, and the Spalart-Allmaras turbulence model. For the asymptotically steady cases under consideration, time integration was accomplished by an Euler implicit backwards difference scheme, with local time stepping to accelerate convergence. Most of the cases in this study were run for 5000 iterations to achieve convergence of forces and moments to within $\pm 0.5\%$ of the average of their last 1000 iterations.

2.3 Dynamic Aeroelastic Analysis

Recently, a dynamic aeroelastic capability was added to the FUN3D solver [16]. For structural dynamics analysis, FUN3D is now capable of being loosely coupled with an

external finite element solver [17], or in the case of the linear structural dynamics used in this study, an internal modal structural solver can be utilized. This modal solver is formulated and implemented in FUN3D in a similar manner to other Langley aeroelastic codes (CAP-TSD [18] and CFL3D [19]). For the computations presented here, the structural modes were obtained via a normal modes analysis (solution 103) with the Finite Element Model (FEM) solver MSC Nastran^{TM} [20]. Modes were interpolated to the surface mesh using the method developed by Samareh [21].

The dynamic analysis was performed in a three-step process. First, the steady CFD solution was obtained on the rigid vehicle. Next, a static aeroelastic solution was obtained by continuing the CFD analysis in a time accurate mode, allowing the structure to deform. A high value of structural damping (0.99) was used so the structure could find its equilibrium position with respect to the mean flow before the dynamic response was started. Finally, for the dynamic response, the damping was set to the expected value (0.00), and the structure was perturbed in generalized velocity for each of the modes included in the structural model. The flow was then solved in the time accurate mode. It should be noted that a user-specified modal motion is available in FUN3D. In this study, for harmonic perturbation, the modal displacement for mode n was computed as:

$$q_n = A_n sin(\omega_n t) \tag{4}$$

where A_n is amplitude, ω_n is frequency, and t is time.

3 AGARD 445.6 WING ANALYSIS

The AGARD 445.6 wing was tested in the Transonic Dynamics Tunnel (TDT) in 1961 [22]. Flutter data from this test has been publicly available for over 20 years and has been widely used for preliminary computational aeroelastic benchmarking. The AGARD wing planform was sidewall-mounted and had a quarter-chord sweep angle of 45 degrees, an aspect ratio of 1.65, a taper ratio of 0.66, a wing semispan of 2.5 feet, a wing root chord of 1.833 feet, and a symmetric airfoil. The wing was flutter tested in both air and R-12 heavy gas test mediums at Mach numbers from 0.34 to 1.14 at zero-degrees angle of attack. Unfortunately, this data set lacks unsteady surface pressure measurements necessary for more extensive code validation.

The FUN3D computations for the AGARD 445.6 wing were performed across the entire Mach number range of the experimental data, assuming both inviscid and viscous flows with air as the working fluid. The first four modes were used in the aeroelastic analysis. Historically, the flutter experimental and numerical results for AGARD 445.6 have been presented in the form of "flutter speed index" and "frequency ratio", which are defined as:

$$flutter\ speed\ index = \frac{V}{b\ \omega_\alpha\ \sqrt{\bar{\mu}}} \quad , \qquad frequency\ ratio = \frac{\omega}{\omega_\alpha} \tag{5}$$

where V is the freestream velocity, b is the wing root semichord, $\bar{\mu}$ is the mass ratio, ω is the flutter frequency, and ω_α is the wing first torsion mode frequency.

The computational process to calculate flutter speed index and the frequency ratio requires multiple steps. First, the rigid steady solution is obtained. Static aeroelastic analysis is not necessary since the wing with the symmetric airfoil is at zero-degrees angle of attack; therefore, the next step is to perform several dynamic aeroelastic FUN3D computations with different values of the dynamic pressure (Q) in the vicinity of the experimental flutter dynamic pressure. The wing response in the form of the time varying generalized variable is then computed and used to calculate the damping ratio from the first bending mode generalized variable time history using the logarithmic decrement method. For the stable solution, the damping ratio is greater than zero, and for the unstable solution, the damping ratio is less than zero. The damping ratio and the dynamic pressure are interpolated, and at zero damping ratio the dynamic pressure is considered to be the flutter dynamic pressure. Once this flutter dynamic pressure is identified, the corresponding flutter frequency is determined via an interpolation of the frequencies at that condition. The computational points and zero damping ratio interpolation process for the Mach = 0.9 and angle of attack $\alpha = 0°$ condition assuming inviscid flow are shown in Figure 1.
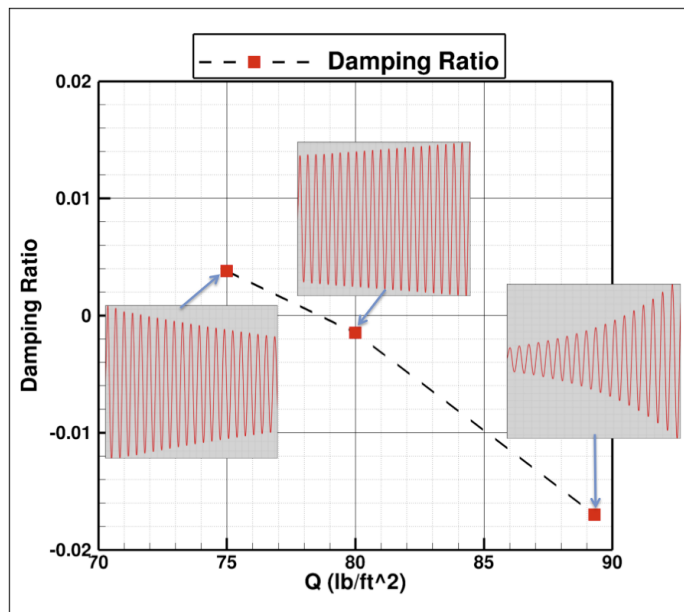
Figure 1: Determination of the AGARD 445.6 wing flutter dynamic pressure via interpolation at Mach = 0.9 and $\alpha = 0°$ assuming inviscid flow in air.

Figures 2(a) and (b) show comparisons among the experimental flutter speed index and frequency ratio values, respectively, and those obtained using FUN3D and those published in the literature [23–26]. In general, in the subsonic flow regime, the computational data matches the experimental data well, while a broad range in the computational data is observed in the transonic and supersonic flow regimes. The FUN3D results in Figure 2 emphasize the importance of the viscous flow assumption near the transonic dip and the necessity to use a fine grid in the supersonic flow regime.

The largest discrepancies between the experimental and the numerical data in Figure 2 occur at the Mach = 1.14 flow condition. Consequently, a grid refinement study was conducted at this condition. Figures 3(a) through 3(d) show the planform and Y = 1 plane views for the baseline and fine grids used in this analysis. These two tetrahedral
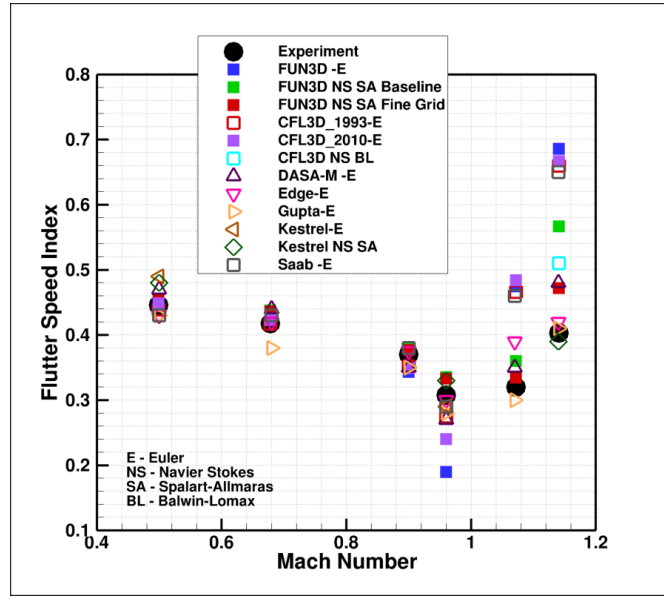
(a) Flutter speed index
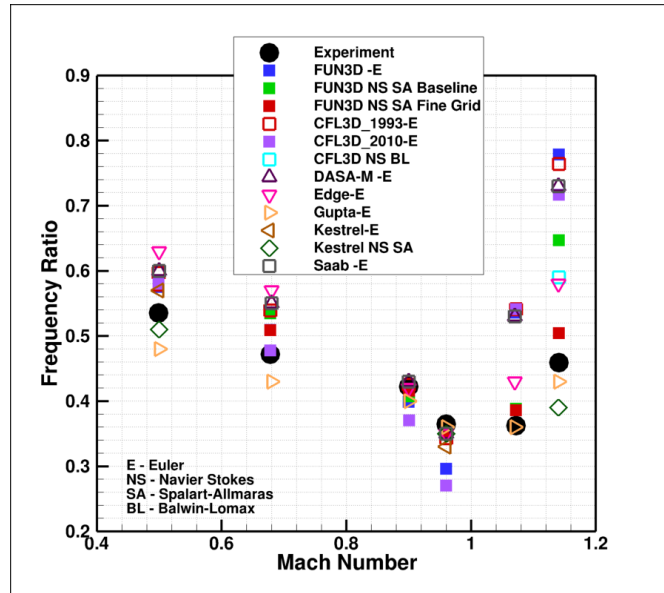
(b) Frequency ratio

Figure 2: Experimental and computational flutter speed index and frequency ratio versus Mach number for the AGARD 445.6 wing.

grids are not in a family of successive grid refinements because of differences in the viscous layer growth rates (as defined in Section 2.1) and local grid refinements. For the baseline grid, the geometric and exponential growth rates were $r_1 = r_2 = 0.08$, while for the fine grid they were $r_1 = 0.08$ and $r_2 = 0.00$. The baseline grid consisted of four million points, and the fine grid consisted of 8 million points. Both grids used the same initial cell height, corresponding to $y^+ = 0.3$, and the length-scale growth rate parameters (Γ_1 and Γ_2) were set to 0.15. Figures 3(e) through 3(h) show surface C_p and Mach contours in the Y = 1 plane. Overall, the grid refinement resulted in better definition of the supersonic flow around the wing (Figure 3(h)) and significantly improved the flutter boundary prediction. Another grid refinement step will be conducted to further verify these results.
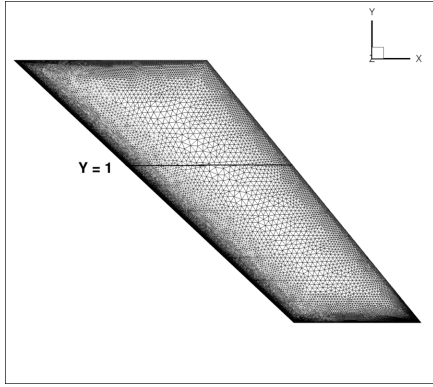
(a) Baseline surface grid
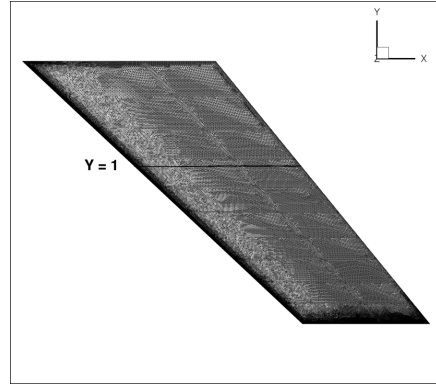
(b) Fine surface grid
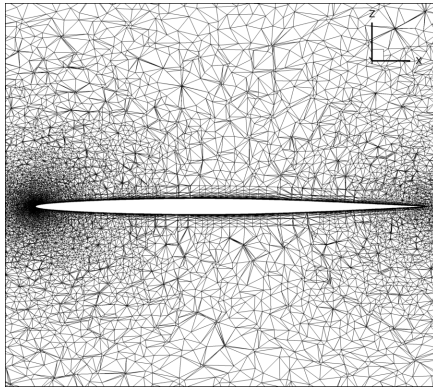
(c) Y = 1 plane for the baseline grid
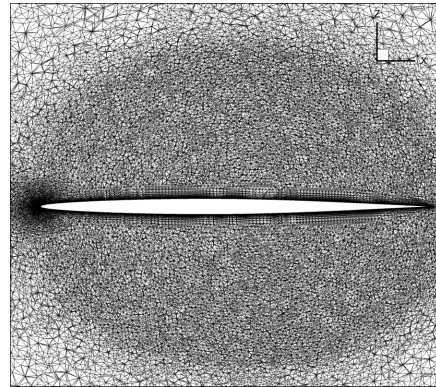
(d) Y = 1 plane for the fine grid
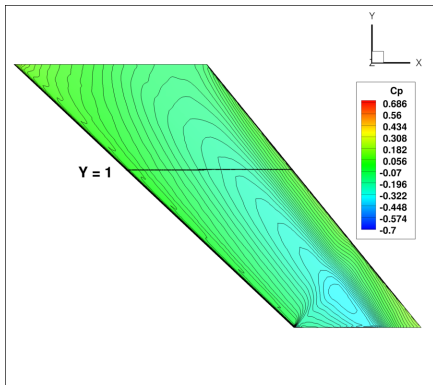
(e) Surface C_p for the baseline grid
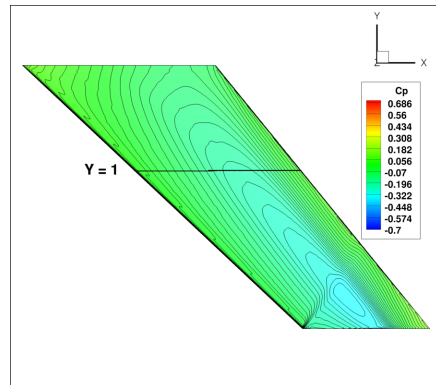
(f) Surface C_p for the fine grid
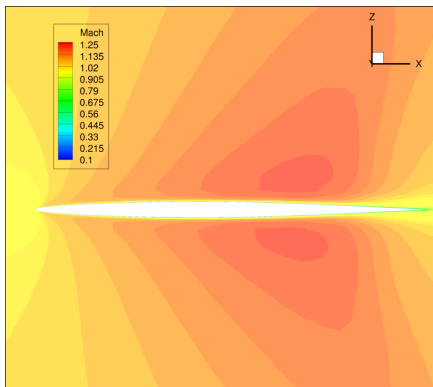
(g) Mach contours in the Y = 1 plane for the baseline grid
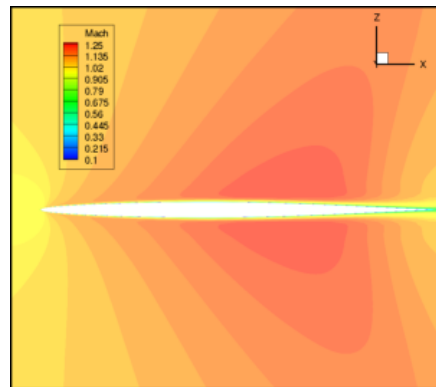
(h) Mach contours in the Y = 1 plane for the fine grid

Figure 3: Baseline and fine grids, surface C_p, and Mach contours in the Y = 1 plane from FUN3D solutions at Mach = 1.14 freestream for the AGARD 445.6 wing.

7

4 HIGH REYNOLDS NUMBER AERO-STRUCTURAL DYNAMICS (HIRENASD) PROJECT

The HIgh REynolds Number Aero-Structural Dynamics (HIRENASD) Project [5–7] was led by Aachen University's Department of Mechanics (LFM) with funding from the German Research Foundation (DFG). It was initiated in 2004 to produce a high-quality transonic aeroelastic data set at realistic flight Reynolds numbers for a large transport-type wing/body configuration and tested in the European Transonic Windtunnel (ETW) in 2006. The HIRENASD wing planform, shown in Figure 4, is a ceiling-mounted, semi-span, clean-wing configuration with a leading-edge sweep of 34 degrees, a span of approximately 1.3 meters, and a mean aerodynamic chord of 0.3445 meters. It consists of three sections. The two outboard sections use an 11-percent thick BAC3-11/RES/30/21 supercritical airfoil. The inboard section uses the same airfoil thickened linearly from 11-percent at its outer edge to 15-percent at the root. To minimize boundary layer interference during testing, a generic fuselage was included. It extended 0.09 meters from the tunnel ceiling and was mechanically isolated from the wing by a labyrinth seal. Extensive measurements were acquired during testing of the HIRENASD model. Instrumentation included a six-component balance, Surface Pattern Tracking (SPT) optical markers for surface deformation measurements on the pressure side of the wing, 11 accelerometers, 28 strain gages, and 259 unsteady pressure transducers. The pressure transducers were distributed along the upper and lower surfaces at seven span sections.
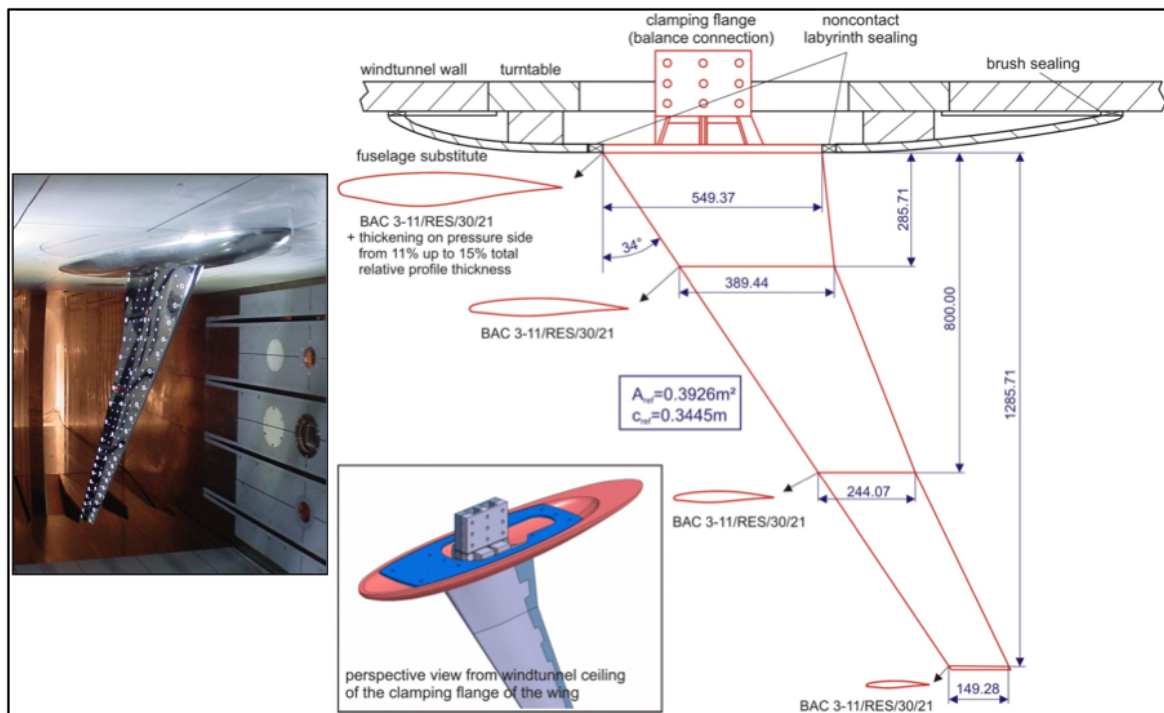
Figure 4: HIRENASD wing model planform, assembly, and ETW installation photo. Dimensions shown are in millimeters.

The HIRENASD test matrix consisted of both static and dynamic measurements at different flow conditions, with variations of Reynolds number from 7 million up to 73 million based on the mean aerodynamic chord and dynamic pressures up to 130,000 pascals at six transonic Mach numbers: 0.70, 0.75, 0.80, 0.83, 0.85, 0.88. The test medium was nitro-

gen. For static testing, pressure distribution and lift and drag coefficients were acquired at various angles of attack. Dynamic testing involved forced vibrations of the wing at the natural frequencies of the first bending, second bending, and first torsion modes and was performed over the range of Reynolds numbers at different angles of attack.

The focus of this paper is on comparing the computational results obtained using FUN3D with the HIRENASD experimental test cases No. 132 for angle-of-attack sweep and No. 159, where the model was harmonically excited at the second bending mode frequency. The rest of this section is organized in the following way. First, the description of the grids used in the analysis is presented. Next, the finite element model and the issues encountered with interpolating the mode shapes to the surface mesh are described. The rigid steady and the static aeroelastic results are then compared together against the experimental data. Next, the harmonic excitation experimental data are compared against the unsteady computational results. Finally, some computational dynamic aeroelastic results are briefly introduced.

4.1 Unstructured Grids

Three unstructured tetrahedral grids with prism elements in the boundary layer were used in this study. The grid parameters, which are based on a Reynolds number of 23.5 million and $c_{ref} = 0.3445$ meter, are shown in Table 1. Grids A and B belong to the same family of grids. Grid C was constructed to investigate the effect of the wind-tunnel ceiling modeled as a viscous surface. In this grid, the location of the outer boundary in the computational domain was reduced from 100 to 30 times the c_{ref}. This change was arbitrary since no information regarding boundary layer growth inside the ETW was readily available. The surface grid extracted from grid A is shown in Figure 5.

	Grid A	Grid B	Grid C
Chordwise Spacing at Wing LE	$0.20\%c_{root}$	$0.07\%c_{root}$	$0.07\%c_{root}$
Chordwise Spacing at Wing TE	$0.10\%c_{root}$	$0.07\%c_{root}$	$0.07\%c_{root}$
Average Cell y^+	0.444	0.296	0.296
Prism Layer Cells	30	30	30
Viscous Wall Spacing Δ_0 (meter)	$1.96E^{-7}$	$1.31E^{-7}$	$1.31E^{-7}$
Grid Size (nodes in millions)	10	30	30
Outer Boundary	$100c_{ref}$	$100c_{ref}$	$30c_{ref}$
Viscous Stretching r_1,r_2	0.02, 0.15	0.02, 0.15	0.02, 0.15
Γ_1,Γ_2	0.15, 0.15	0.15, 0.15	0.15, 0.15
Wind-Tunnel Ceiling Boundary Cond.	Symmetry	Symmetry	Viscous

Table 1: VGRID parameters for HIRENASD configuration grids.

4.2 Finite Element Model

Two different Finite Element Models (FEMs) are available from the HIRENASD website [27]. Both are modeled with uniform solid elements. One FEM uses NASTRAN hexagonal elements with over 200,000 grid points, while the other uses NASTRAN tetrahedral elements with approximately 170,000 grid points. The two FEMs yield slightly different modal frequencies. However, these differences are small (less than 1.3 percent),
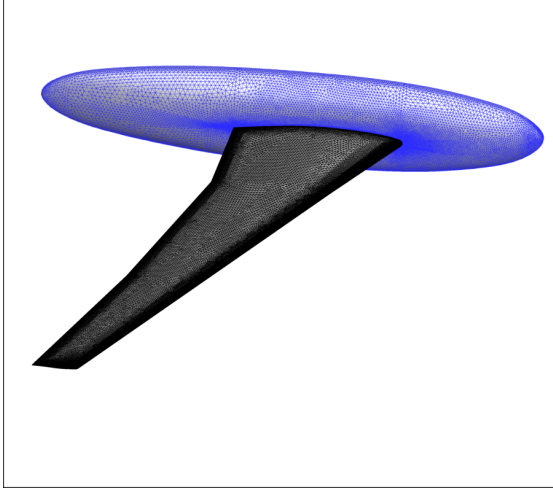
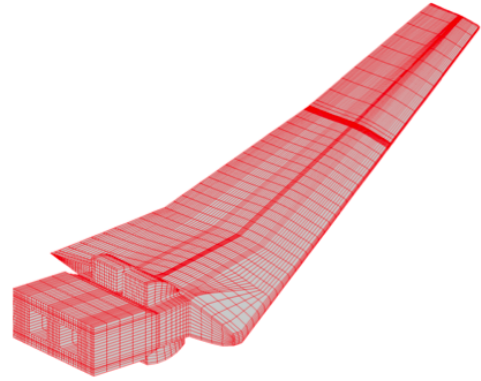Figure 5: Grid A surface grid used in FUN3D analysis for the HIRENASD configuration.

Figure 6: FEM with hexagonal elements used in modal analysis for the HIRENASD configuration.

and the first ten modes are nearly identical. Modal analyses using the available FEMs were performed, where the material properties were varied to investigate their impact on modal frequencies. These frequencies were plotted (not shown here) against Young's Modulus, which was a function of temperature. The resulting variations of the modal frequencies and mode shapes were assessed to be negligible. For the aeroelastic analyses presented in this paper, the first ten modes extracted from the NASTRAN model with hexagonal elements, shown in Figure 6, were used.

4.3 Rigid Steady and Static Aeroelastic Analyses

The rigid steady solutions corresponding to HIRENASD test case No. 132 at Mach = 0.8 and Re = 7 million were obtained at five angles of attack for grids A and B (-1.5, 0.0, 1.5, 3.0, and 4.5 deg) and one angle of attack for grid C (1.5 deg). The rigid steady solutions were then used as initial conditions for the corresponding static aeroelastic solutions, which in turn were obtained by running FUN3D in the unsteady flow mode with the linear structural solver, where the structural damping was set to a large value. The solution process required that the mode shapes be interpolated to the surface grid. In the first attempt of the static aeroelastic analysis, the mode shapes were interpolated to a surface grid consisting of the wing geometry only, even though the wing was attached to the fuselage. In this process, FUN3D failed in the beginning of the unsteady flow solution due to the negative volumes at the wing-fuselage junction. It was deduced that this failure was caused by the discontinuity in mode shape at this location, resulting from the geometric differences between structural model and the wing-only shape. A new method was subsequently developed, where initially the mode shapes were interpolated to both the wing and fuselage. The mode shapes were then set to zero on the fuselage, with the exception of a very narrow region near the wing and fuselage junction. In this region, the mode shapes were linearly interpolated from zero to the nominal value at the root of the wing. This second method resulted in successful execution of the flow solver. Figure 7 depicts an example of the mode shape interpolation process from FEM to CFD surface mesh for the second bending mode (mode 2). Figure 7(a) shows mode 2 as extracted

from the FEM, Figure 7(b) shows the interpolation of mode 2 onto the wing-only surface, which resulted in flow solver failure due to the negative volumes, and Figure 7(c) shows the interpolation of mode 2 onto the wing and fuselage, which resulted in the successful execution of FUN3D.

(a) Mode 2 from FEM

(b) Mode 2 interpolation to wing-only, which resulted in negative volumes

(c) Mode 2 interpolation to wing and fuselage, resulting in flow solver successful execution
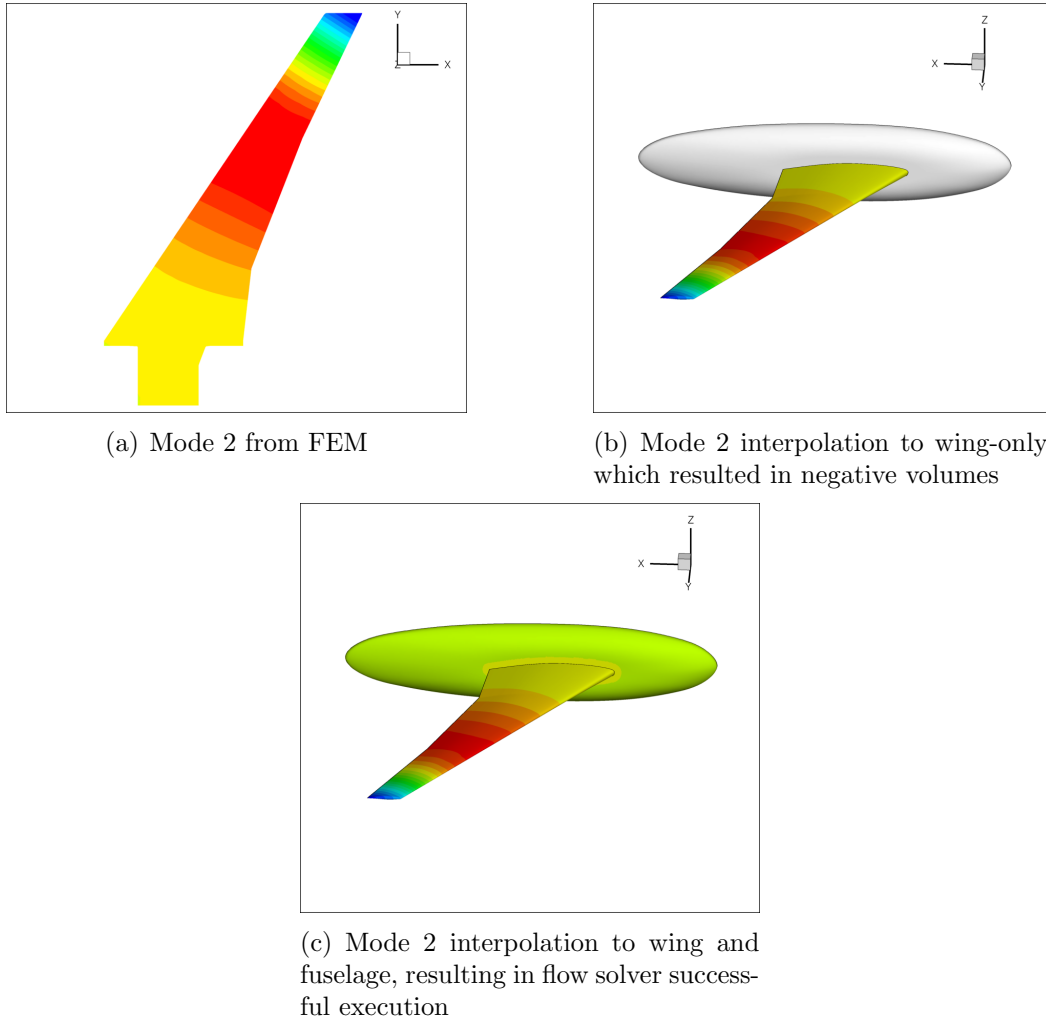
Figure 7: Example of the mode shape interpolation process from FEM into CFD surface mesh for the HIRENASD configuration.

The aerodynamic coefficients obtained from rigid steady and static aeroelastic calculations for grids A, B, and C are shown in Table 2. A decrease in computed drag coefficient is observed between grid A and grids B and C. Also, a small lift decrement exists between the rigid steady and deformed (static aeroelastic) configurations. The wing tip displacements calculated using grids A and B compared with the experimental SPT data are shown in Figure 8. The experimental and computational data compare very well. The wing twist experimental SPT data was not available when this document was written; therefore, a corresponding plot of the experimental versus computational spanwise wing twist is not presented. However, the computational wing twist values ($\Delta\alpha$) at the wing tip are shown in Table 3.

As previously mentioned, the HIRENASD experimental unsteady pressure data was collected at seven span sections, which are identified in Figure 9. Figure 10 presents the C_p

	Grid A Rigid Steady Solution			Grid A Static Aeroelastic Solution		
AoA (°)	C_L	C_D	C_M	C_L	C_D	C_M
-1.5	0.0145	0.0137	-0.0964	0.0099	0.0138	-0.0887
0.0	0.1811	0.0132	-0.3178	0.1703	0.0131	-0.2997
1.5	0.3542	0.0173	-0.5516	0.3373	0.0166	-0.5231
3.0	0.5218	0.0260	-0.7770	0.4996	0.0242	-0.7399
4.5	0.6493	0.0408	-0.9266	0.6373	0.0372	-0.9118
	Grid B Rigid Steady Solution			Grid B Static Aeroelastic Solution		
AoA (°)	C_L	C_D	C_M	C_L	C_D	C_M
-1.5	0.0135	0.0117	-0.0974	0.0087	0.0117	-0.0894
0.0	0.1806	0.0113	-0.3204	0.1693	0.0111	-0.3012
1.5	0.3544	0.0154	-0.5574	0.3366	0.0147	-0.5271
3.0	0.5190	0.0237	-0.7794	0.4964	0.0219	-0.7416
4.5	0.6304	0.0373	-0.8954	0.6236	0.0337	-0.8927
	Grid C Rigid Steady Solution			Grid C Static Aeroelastic Solution		
AoA (°)	C_L	C_D	C_M	C_L	C_D	C_M
1.5	0.3469	0.0146	-0.5461	0.3294	0.0140	-0.5163

Table 2: Computed aerodynamic coefficients for grids A, B, and C (rigid steady and deformed solutions): HIRENASD test case No. 132, Mach = 0.8, Re = 7 million.
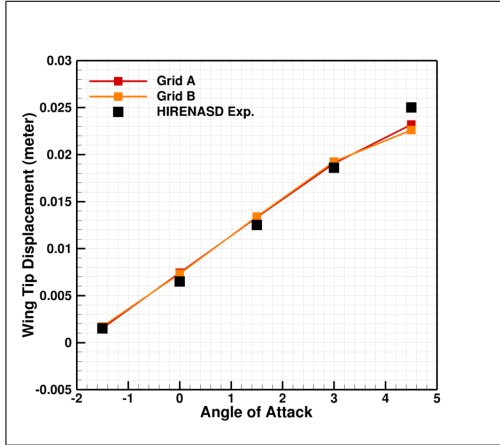
Figure 8: Wing tip displacements for HIRENASD test case No. 132, Mach = 0.8, Re = 7 million.
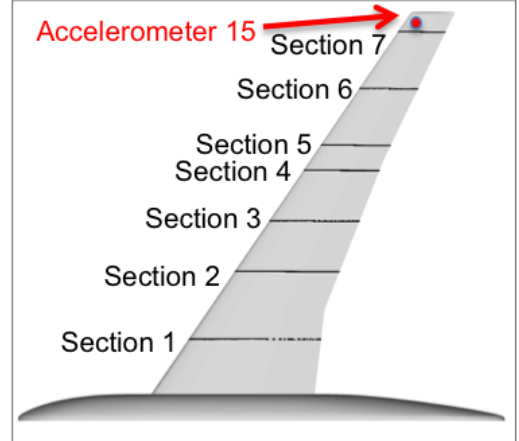
Figure 9: HIRENASD span sections 1-7 and accelerometer 15.

results at sections 1, 2, 5, and 7 for grids A, B, and C obtained from the rigid steady and static aeroelastic solutions. As shown in Figures 10(a) and (b) at section 1 for grids A and B, the computed C_p values have a very similar distribution to the experimental data, but the computed shock appears to be stronger and further aft on the wing for both grids. The grid C solution shown in Figure 10(c) captures the shock location very well. This suggests that modeling the tunnel wall as a viscous surface and thus capturing the boundary layer does have some influence on the wing surface pressure near the ceiling. The computed C_p at section 2 matches the experimental data quite well for all three grids, as shown in Figures 10(d)-(f). The largest discrepancy between the experimental and computational data is observed at section 5. Neumann [28] showed that the shape of

	Grid A	Static Aero.	Solution	Grid B	Static Aero.	Solution
AoA (°)	Δz_{LE} (mm)	Δz_{TE} (mm)	$\Delta \alpha$ (°)	Δz_{LE} (mm)	Δz_{TE} (mm)	$\Delta \alpha$ (°)
-1.5	1.12	1.93	-0.32	1.51	1.90	-0.15
0.0	7.21	7.64	-0.17	6.92	7.71	-0.30
1.5	12.89	13.74	-0.33	12.78	14.02	-0.48
3.0	18.43	19.68	-0.49	18.42	20.07	-0.64
4.5	22.43	23.93	-0.59	21.69	23.51	-0.71

Table 3: Computed leading- and trailing-edge displacements and the wing twist for grids A and B: HIRE-NASD test case No. 132, Mach = 0.8, Re = 7 million.

the trailing edge of the HIRENASD wing has a significant effect on C_p at section 5. He compared computational results using the Tau [29] code where the trailing edge of the wing was considered to be either sharp, blunt, or blunt with rounded corners, which was the shape used to generate grids for the FUN3D computations. Neumann's results for the blunt trailing edge with rounded corners (not shown here) match the solutions presented in Figures 10(g)-(i).

4.4 Harmonic Excitation Analysis

The HIRENASD experimental harmonic excitation tests were conducted to measure the interaction between aerodynamics and modal excitations. For test case No. 159 (Mach = 0.8, Re = 7 million), the model was excited at 78.9 Hz, which closely corresponds to the second bending mode frequency. Numerically, the modal excitation is accomplished using Equation 4. The unsteady solutions were restarted from the static aeroelastic solutions and were run for six cycles, with 64 time steps per cycle and 25 subiterations per time step. A drop in the residuals of three to five orders of magnitude was obtained within 25 subiterations. The unsteady surface pressure and surface shape were collected at each time step for four cycles. The results were post-processed to produce the transfer function estimate of pressure due to displacement at the specified locations. For this study, the location of the displacement used in the analysis coincided with the location of accelerometer 15, which is shown in Figure 9. The displacement value was normalized by the reference chord. Figures 11 and 12 show the resulting C_p magnitude and phase plots, respectively, for sections 1 through 7 for grids A, B, and C. For these calculations, the peak-to-peak amplitude at accelerometer location 15 was 8.5 mm. The shock locations at sections 1-5 are predicted quite well, but the prediction is poor near the wing tip. Figure 13 shows the C_p magnitude plots where the computational solutions were obtained with grid A for three different excitation amplitudes: Amp1 = 4.25mm, Amp2 = 8.5mm, and Amp3 = 85mm. Clearly, the computational excitation amplitude has an effect on the numerical results. Similarly, Figure 14 shows the magnitude plots where three different methods within FUN3D were used to obtain the solution on grid A: (1) LDFSS for inviscid fluxes with augmented van Leer limiter and Spalart-Allmaras turbulence model (labeled as 'Grid A'), (2) LDFSS for inviscid fluxes with augmented van Leer limiter and SST turbulence model (labeled as 'Grid A SST'), and (3) Roe scheme with Venkatakrishnan limiter and Spalart-Allmaras turbulence model (labeled as 'Grid A Roe SA'). The results show that the solution is more dependent on the choice of the inviscid flux method or limiter than it is on the choice of turbulence model. Future analysis will address the effects of the time step size on the surface pressure calculation.
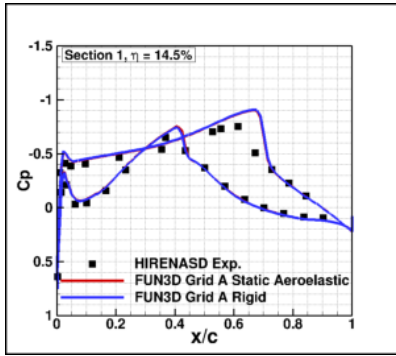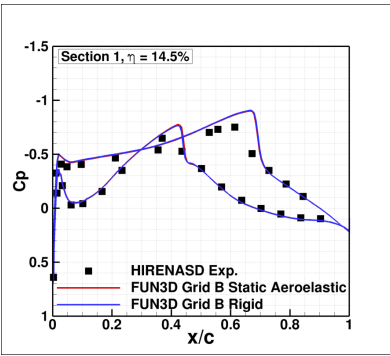
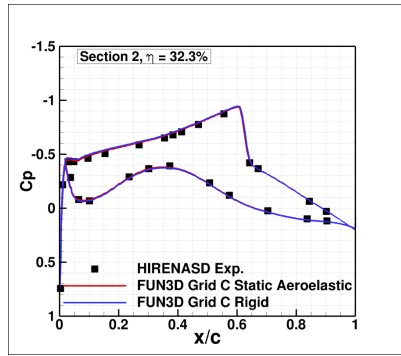(a) Grid A Section 1   (b) Grid B Section 1   (c) Grid C Section 1
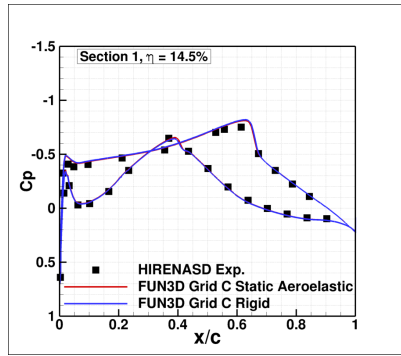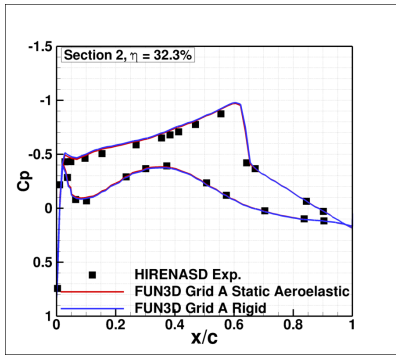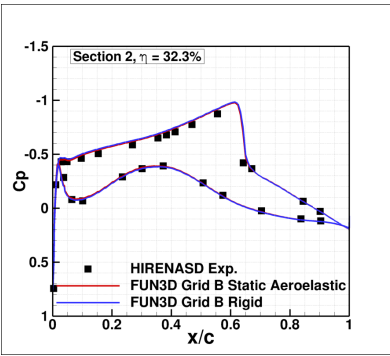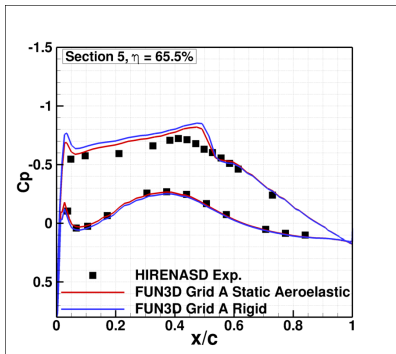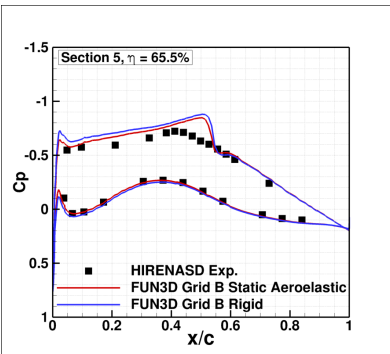
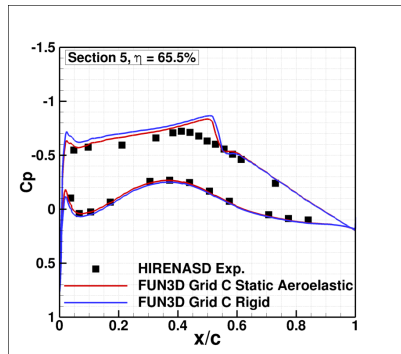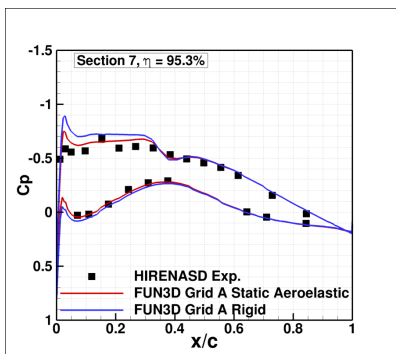(d) Grid A Section 2   (e) Grid B Section 2   (f) Grid C Section 2
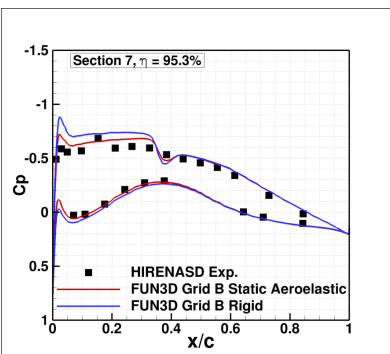
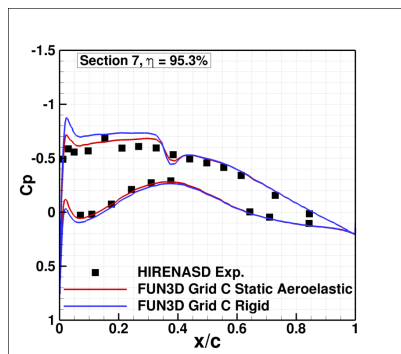(g) Grid A Section 5   (h) Grid B Section 5   (i) Grid C Section 5
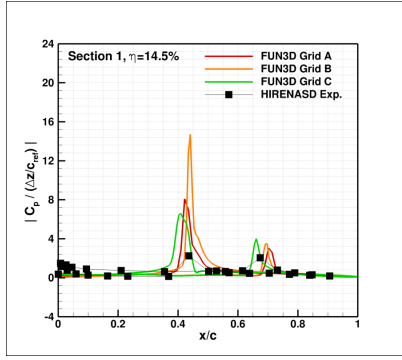
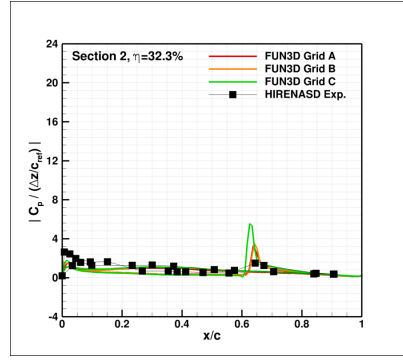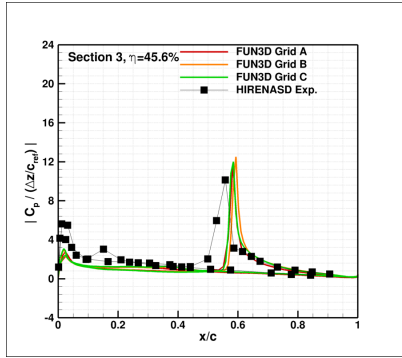(j) Grid A Section 7   (k) Grid B Section 7   (l) Grid C Section 7

Figure 10: Rigid steady and static aeroelastic surface pressure comparison for grids A, B, and C at sections 1, 2, 5, and 7 for HIRENASD test case No. 132, Mach = 0.8, Re = 7 million.
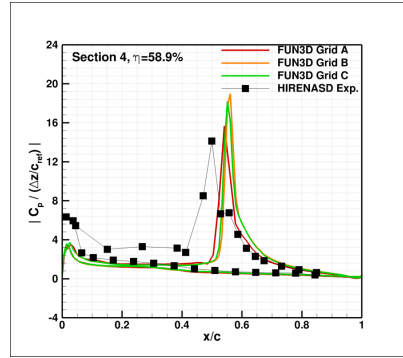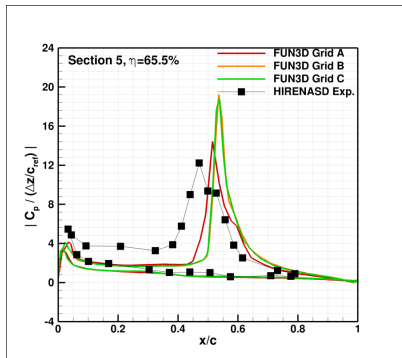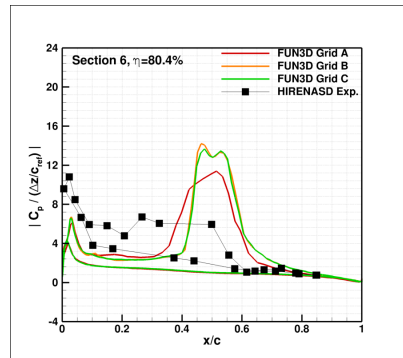
(a) Section 1

(b) Section 2

(c) Section 3
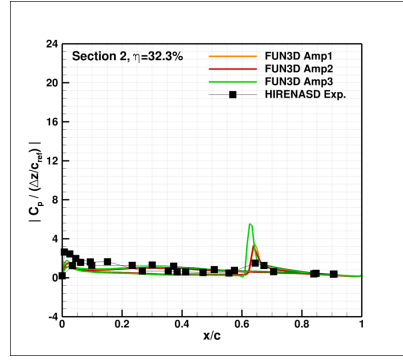

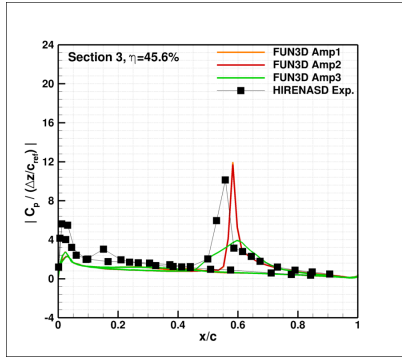(d) Section 4

(e) Section 5
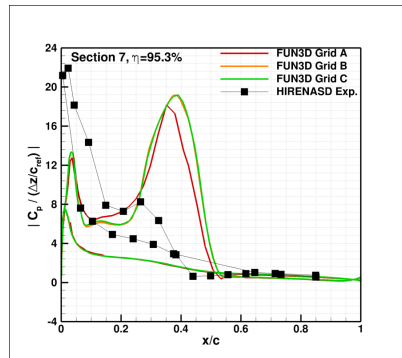
(f) Section 6

(g) Section 7

Figure 11: Magnitudes of the transfer function of the pressure coefficient due to the displacement at accelerometer 15 for grids A, B, and C; HIRENASD test case No. 159, Mach = 0.8, Re = 7 million.
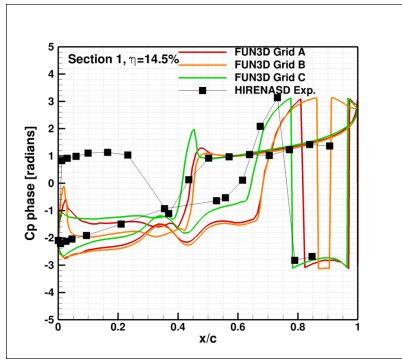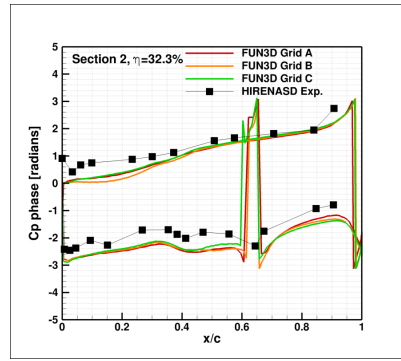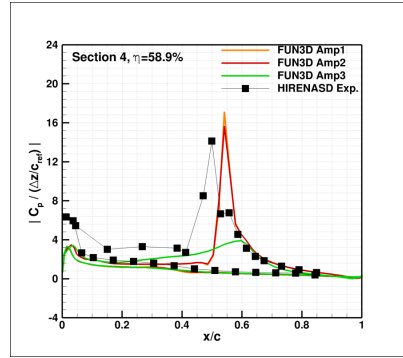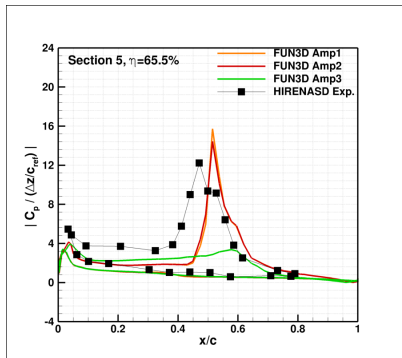
(a) Section 1
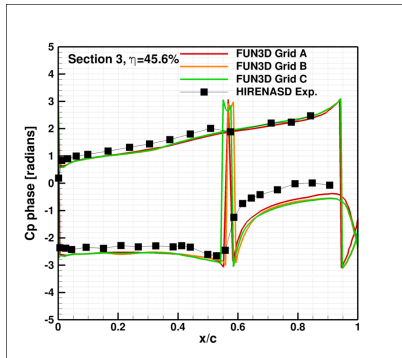
(b) Section 2
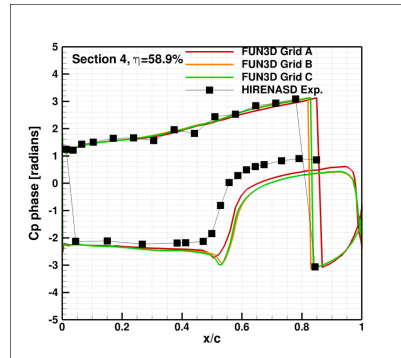
(c) Section 3
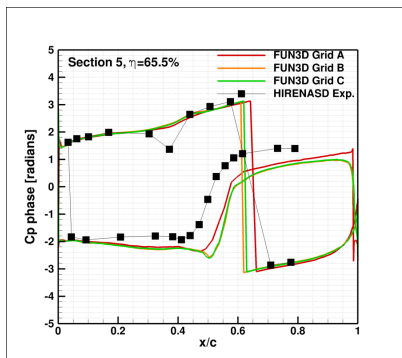
(d) Section 4
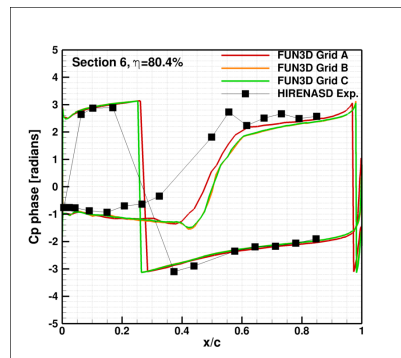
(e) Section 5
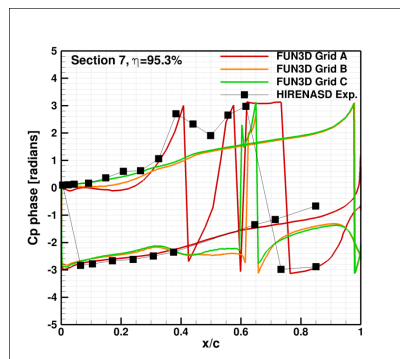
(f) Section 6

(g) Section 7

Figure 12: Phase plots of the transfer function of the pressure coefficient due to the displacement at accelerometer 15 for grids A, B, and C; HIRENASD test case No. 159, Mach = 0.8, Re = 7 million.
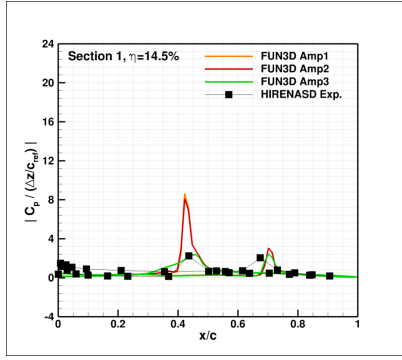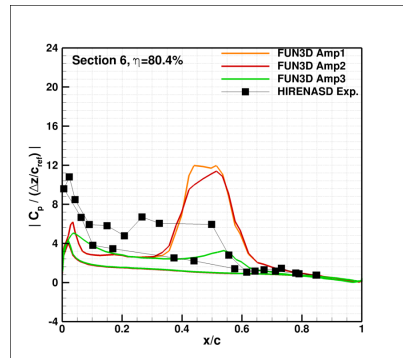
(a) Section 1

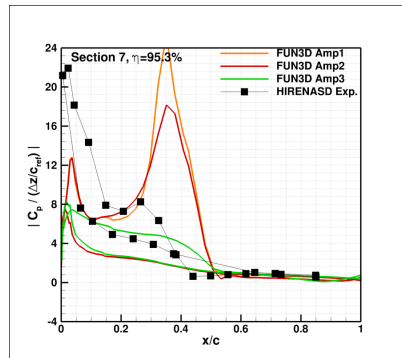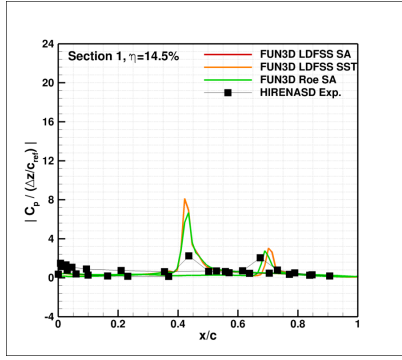(b) Section 2

(c) Section 3

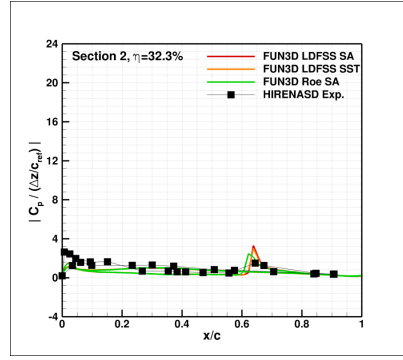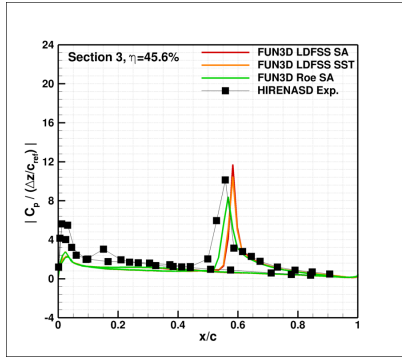(d) Section 4

(e) Section 5

(f) Section 6

(g) Section 7

Figure 13: Magnitudes of the transfer function of the pressure coefficient due to the displacement at accelerometer 15 for grid A at three excitation amplitudes; HIRENASD test case No. 159, Mach = 0.8, Re = 7 million.
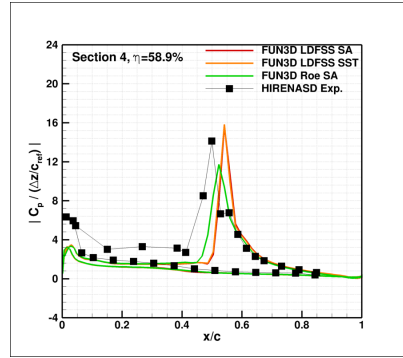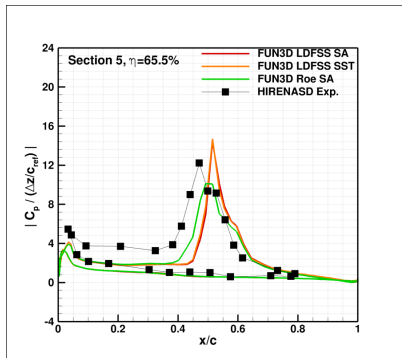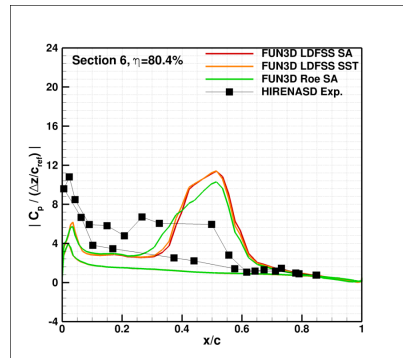
(a) Section 1

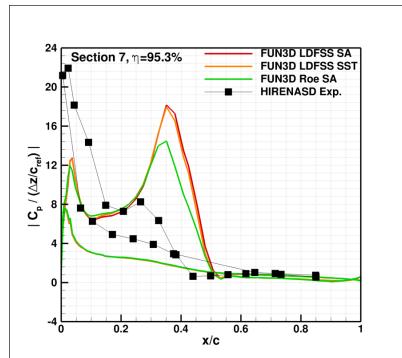(b) Section 2

(c) Section 3

(d) Section 4

(e) Section 5

(f) Section 6

(g) Section 7

Figure 14: Magnitudes of the transfer function of the pressure coefficient due to the displacement at accelerometer 15 for grid A for different flow solver options; HIRENASD test case No. 159, Mach = 0.8, Re = 7 million.

4.5 Dynamic Aeroelastic Analysis

The dynamic aeroelastic analysis capability in FUN3D was exercised using grid A to investigate the dynamic aeroelastic behavior of the HIRENASD configuration at flow conditions corresponding to test case No. 159. In this simulation, the dynamic analysis was re-started from the static aeroelastic solution by setting the structural damping to zero value and perturbing the structure in generalized velocity for each of the modes used. Ten modes were perturbed with the same value of the initial generalized velocity. The time step was set sufficiently small such that the cycles of the first and tenth modal frequencies were resolved into 1205 time steps and 51 time steps, respectively. The generalized coordinates for modes 1 through 10 versus time are shown in Figure 15. The solution shows that all modes are damped.
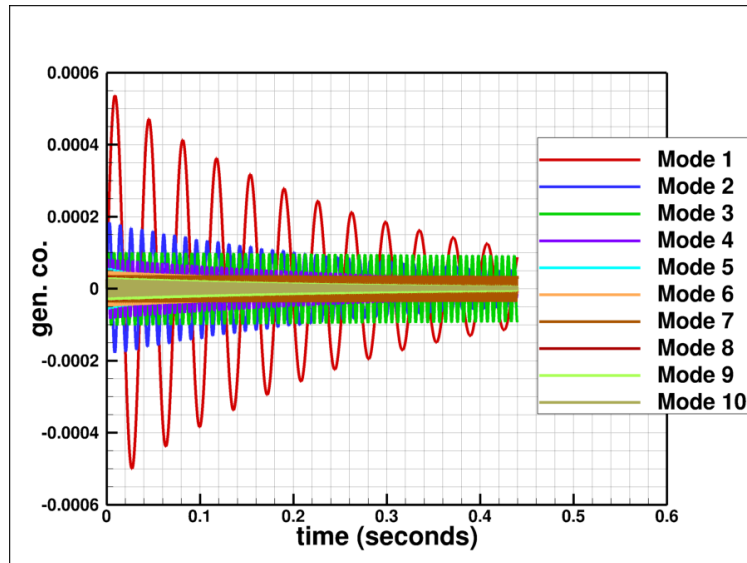

Figure 15: Generalized coordinate as a function of time for modes 1-6; HIRENASD configuration, Mach = 0.8, Re = 7 million.

5 CONCLUDING REMARKS

Reynolds-Averaged Navier-Stokes analyses, including static aeroelastic, forced excitation, and dynamic aeroelastic computations, were performed as part of the validation process of the NASA Langley FUN3D software for two configurations: the AGARD 445.6 wing and HIRENASD. The AGARD 445.6 wing analysis showed that FUN3D could predict the flutter boundary well for this planform. The analysis also showed the importance of a viscous flow assumption to accurately predict the flutter boundary at transonic speeds near the transonic dip. In addition, a highly resolved grid was required to match the experimental data at the supersonic speeds.

The HIRENASD configuration analysis showed that FUN3D predictions matched the experimental data well. The computed static aeroelastic wing tip displacement and the magnitude and phase of the transfer function of the pressure coefficient due to normalized deflection showed very satisfactory results. Additional grid convergence and computational time step sensitivity iterations are needed.

Lessons learned from the analysis of the HIRENASD configuration have resulted in several

recommendations for the first Aeroelastic Prediction Workshop, with the goal of reducing uncertainty across participant-generated results. First, common gridding guidelines that establish the definition of a grid family need to be developed. A common finite element model and a common method of interpolating modes to the surface grid must also be established. To avoid ambiguities in the surface definition, such as the wing's trailing-edge geometry, a common baseline geometry is needed. And finally, a common method for post-processing the time-accurate data needs to be defined.

6 ACKNOWLEDGMENTS

7 REFERENCES

[1] http://fun3d.larc.nasa.gov. NASA Langley Research Center, November 2010.

[2] http://aaac.larc.nasa.gov/tsab/cfdlarc/aiaa-dpw/. August 2010.

[3] http://hiliftpw.larc.nasa.gov/. August 2010.

[4] Heeg, J., Ballmann, J., Bhatia, K., et al. Plans for an Aeroelastic Prediction Workshop. IFASD Paper 2011-110.

[5] Ballmann, J., Dafnis, A., Korsch, H., et al. Experimental Analysis of High Reynolds Number Aero-Structural Dynamics in ETW. AIAA Paper 2008-841.

[6] Ballmann, J., Boucke, A., Dickopp, C., et al. Results of Dynamic Experiments in the HIRENASD Project and Analysis of Observed Unsteady Processes. IFASD Paper 2009-103.

[7] Ballmann, J., Dafnis, A., Braun, C., et al. The HIRENASD Project: High Reynolds Number Aerostructural Dynamics Experiments in the European Transonic Windtunnel (ETW). ICAS Paper 2006-726.

[8] Pirzadeh, S. Z. Advanced Unstructured Grid Generation for Complex Aerodynamic Applications. AIAA Paper 2008-7178.

[9] Samareh, J. A. Unstructured Grids on NURBS Surfaces. AIAA Paper 1993-3454.

[10] Spalart, P. R. and Allmaras, S. R. A One-Equation Turbulence Model for Aerodynamic Flows. *La Recherche Aerospatiale*, No. 1, 1994, pp 5–21.

[11] Menter, F. Two-Equation Eddy-Viscosity Turbulence Models for Engineering Applications. *AIAA Journal.* Vol. 32, No. 8, 1994, pp 1598-1605.

[12] Vatsa, V. N. and White, J. A. Calibration of a Unified Flux Limiter for Ares-Class Launch Vehicles from Subsonic to Supersonic Speeds. JANNAF Paper 2009.

[13] Venkatakrishnan, V. Convergence to Steady State Solutions of the Euler Equations on Unstructured Grids with Limiter. *Journal of Computational Physics.* Vol. 118, No. 1, 1995.

[14] Edwards, J. R. A Low-Diffusion Flux-Splitting Scheme for Navier-Stokes Calculations. AIAA Paper 1995–1703.

[15] Roe, P. L. Approximate Riemann Solvers, Parameter Vectors, and Difference Schemes. *Journal of Computational Physics.* Vol. 43, No. 2, 1981.

[16] Biedron, R. T. and Thomas, J. L. Recent Enhancements to the FUN3D Flow Solver for Moving-Mesh Applications. AIAA Paper 2009-1360.

[17] Biedron, R. T. and Lee-Rausch, E. M. Rotor Airloads Prediction Using Unstructured Meshes and Loose CFD/CSD Coupling. AIAA Paper 2008-7341.

[18] Batina, J. T., Seidel, D. A., Bland, S. R., et al. Unsteady Transonic Flow Calculations for Realistic Aircraft Configurations. AIAA Paper 1987-0850.

[19] Bartels, R. E., Rumsey, C. L., and Biedron, R. T. CFL3D Version 6.4 - General Usage and Aeroelastic Analysis. NASA TM 2006-214301 March 2006.

[20] http://www.mscsoftware.com/. MSC Software, Santa Ana, CA 2008.

[21] Samareh, J. A. Discrete Data Transfer Technique for Fluid-Structure Interaction. AIAA Paper 2007-4309.

[22] Yates, C. E., Land, N. S., and Foughner, J. T. Measured and Calculated Subsonic and Transonic Flutter Characteristics of a 45deg Sweptback Wing Planform in Air and in Freon-12 in the Langley Transonic Dynamics Tunnel. NASA technical Note D-1616, March 1963.

[23] Lee-Rausch, E. M. and Batina, J. T. Calculation of AGARD Wing 445.6 Flutter Using Navier-Stokes Aerodynamics. AIAA Paper 1993-3476.

[24] Lee-Rausch, E. M. and Batina, J. T. Wing Flutter Boundary Prediction Using Unsteady Euler Aerodynamic Method. *Journal of Aircraft.* Vol. 32, No. 3, 1995.

[25] Gupta, K. K. Development of a Finite Element Aeroelastic Analysis Capability. *Journal of Aircraft.* Vol. 33, No. 5, 1996.

[26] Pahlavanloo, P. Dynamic Aeroelastic Simulation of the AGARD 445.6 Wing Using Edge. Technical Report FOI-R-2259-SE, April 2007.

[27] https://heinrich.lufmech.rwth-aachen.de/en/. Aachen University, June 2010.

[28] Neumann, J., Nitzsche, J., and Voss, R. Aeroelastic Analysis by Coupled Non-linear Time Domain Simulation. RTO-MP-AVT-154 2008.

[29] Schwamborn, D., Gerhold, T., and Heinrich, R. The DLR TAU-CODE: Recent Applications in Research and Industry. Tech. rep. Technical Report at European Conference on Computational Fluid Dynamics, ECCOMAS CFD 2006.